Int. J. Bio-Inorg. Hybr. Nanomater., 10(3): 121-134, Autumn 2021

REVIEW PAPER

Synthesis, properties, and applications of magnetic graphene oxide/ nanocomposites and their photocatalytic activity under visible light irradiation: A Review

A. Zamani[1], M. Seyed Sadjadi[2], A. Mahjoub[3*], M. Yousefi[4] and N. Farhadyar[5]*

[1,2,4] *Department of Chemistry, Science and Research Branch, Islamic Azad University, Tehran, Iran*
[3] *Department of Chemistry, Tarbiat Modares University, Tehran, Iran*
[5] *Department of Chemistry, Varamin Pishva Branch, Islamic Azad University, Varamin, Iran*

Received: 11 January 2021; Accepted: 14 March 2021

ABSTRACT: Graphene oxide is an emanating nanoparticle with diverse applications for energy storage, conversation and industrial wastewater treatment (adsorbent and photocatalysts) due to their outstanding electrical, thermal and chemical attributes.graphene oxide-based nanocomposites a hot area of investigation in the past decade because of their considerable mechanical, electrical, thermal, and barrier properties. Magnetic graphene oxide nanocomposites were prepared via a facile co-precipitation and hydrothermal methods and characterized by X-ray powder diffraction (XRD), Transmission electron microscopy (TEM), field emission scanning electron microscopy (FESEM) and techniques and Bruner-Emmett-Teller (BET). The nanoparticles were found to have a size of 20-60 nm and were spread out on the graphene oxide nanosheets. Magnetic studies demonstrated that graphene oxide nanocomposites can be easily separated from the solution by an external magnetic field. The photocatalytic degradation of Congo red dye (CR) was evaluated based on the removal of Congo red (CR) in aqueous solution under visible light irradiation. The photocatalytic activity was affected by the structural and optical properties as well as the surface area of the samples. Compared with pure nanocomposites, the $MnFe_2O_4$@ZnO-GO nanocomposite compare to $ZnFe_2O_4$@MnO-GO nanocomposite displayed a high photocatalytic activity on the photodegradation of Congo red. The prepared graphene oxide nanocomposite can be potentially applied as a visible-light responsive catalyst and magnetically separable photocatalyst.

Keywords: *Co-precipitation and hydrothermal methods; Congo red; Degradation; Magnetic graphene oxide nanocomposites; Photocatalytic activity.*

INTRODUCTION

In recent decades, environmental pollution and its related effects have studied significant problems that increasingly confront human societies [1]. Because of the diversity of manufactured products, the wastewater, including pollutants has changed into a worldwide public health subject [2–4]. Textile industries are the most specified sections in the world which uses dye to color the fabrics. The presence of organic pollutants in water is a serious threat to the public health for human and wildlife because of their high toxicity [5-7]. Dyes pollutants are transferred by adsorption onto the absorbent, and activated carbon is highly effective in

(*) Corresponding Author - e-mail: m.s.sadjad@gmail.com & mahjouba@modares.ac.ir

the removal of dyes [8]. This is considerable because the acid functional group presence in azo and diazo dyes prevents them from being adsorbed by low-cost absorbent. However, activated carbon is not encouraging due to its heavy cost [9]. Ddifferent semiconductor photocatalysts have been presented for the degradation of organic pollutants. Among them, manganese oxide (MnO) is a semiconductor with a wide band gap width (3.9±0/4 eV) at room temperature [8]. Manganese oxides, containing MnO, MnO_2, and Mn_3O_4, are appealing composites and have been employed in wastewater treatment, catalysis, sensors, supercapacitors and alkaline and rechargeable batteries. Especially, MnO and MnO_2 nanomaterials have done great interest as anode materials in Li-ion batteries (LIBs) for their high theoretical capacity, low cost, environmental benefit and outstanding properties [9]. Zinc Ferrite ($ZnFe_2O_4$) displayed superparamagnetic behavior, and it has potential use in many areas, such as photocatalysis, magnetic resonance imagery (MRI), Li-ion batteries and gas sensors [10]. Iron oxides are very common nanoparticle and they are prevalent in nature and readily synthesized in the lab. Almost all over of the global system atmosphere, biosphere, hydrosphere, and lithosphere, iron oxides present [11]. Among Magnetic nanocomposites, Spinel ferrites as $MnFe_2O_4$ are chemically and thermally stable magnetic nanocomposites with small band gaps About 2 eV which leading to high photocatalytic performance under visible light irradiation [12, 13]. Also, Zinc oxide (ZnO) nanoparticle is a semiconductor with a wide band gap width (3.37 eV) and large excitation binding energy (60 meV) at room temperature, which lead to ZnO has been applied widely in the degradation of dye pollutant [14]. Graphene, an atomic sheet of sp2 bonded carbon atoms, with considerable electrical conductivity, high chemical and thermal stability, excellent absorptivity, high transparency and large specific surface area, constitutes an excellent cloth for the adsorption of many pollutants [15]. Graphene oxide can be applied as an ideal high-performance candidate for the charge migration during the photocatalysis process. Layers of graphene oxide consist of several oxidizing groups like hydroxyl, epoxides, carbonyl and carboxyl at the basal planes as good as at the edges. These groups can be reduced with the help of appropriate reducing agents to generate highly reduced graphene oxide sheets. In this investigation, we made an attempt to synthesize reduced graphene oxide films by oxidation of graphite to form graphene oxide followed by exfoliation and reduction in GO. The main difficulty of pure semiconductor photocatalysts is that the photogenerated electron–hole pairs have faster recombination rates, which will reduce the photocatalytic performance of the semiconductor photocatalysts [16, 17]. One of the impressive ways to solve this problem is to create semiconductor nanoparticles, which will make simple the charge migration [18]. A few research studies have presented on metal oxide nanocomposites and nanocomposites with graphene and graphene derivatives; however, these presented composites endure from low- capability photocatalysis. There are some researches such as (Nd-ZrO_2–GO) nanocomposite presented the degradation of only 20 ppm eosin Y dye in 180 min [19], $PbTiO_3$/carbon quantum dots binary nano hybrids (decomposes rhodamine B dye 5 ppm in 150 min under visible light) [20], Thulium titanate/polyaniline nanoparticles(decomposes rhodamine B dye 10 ppm in 200 min under visible light) [21], composite of $CuWO_4$/NiO (decomposes MO dye in aqueous solution under UV irradiation) [22], $YbVO_4$/$CuWO_4$ nanocomposites(decomposes methylene blue dye 50 ppm in 120 min under visible light) [23], GO–ZrO_2 nanocomposite (decomposes rhodamine B 30 ppm in 105 min) [24]. $ZnFe_2O_4$@MnO-GO and Zn-Fe_2O_4@MnO nanocomposites (decomposes dye Congo red 10 ppm in 35 min) [25]. GO– $MnFe_2O_4$@ZnO and $MnFe_2O_4$@ZnO nanocomposites (decomposes dye Congo red 10 ppm in 35 min) [26]. In spite of a large number of papers published on nanocomposites photocatalytic performance, photocatalytic degradation of nanocomposites -graphene oxide and nanocomposites–reduced graphene oxide nanocomposites for degradation of Congo red dye under the visible light irradiation have been investigated. In this research, synthesis of the nanoparticles decorated on the surface reduced graphene oxide (RGO) and graphene oxide (GO). Therefore, nanocomposites -graphene oxide were accomplished. Magnetic nanocomposites-graphene oxide was prepared by the hydrothermal and co-precipitation methods. The microstructure, optical properties and magnetic properties of the synthesized

nanoparticles were studied. In addition, percent degradation and degradation kinetics have been considered in detail.

Synthesis of graphene oxide

Graphene oxide (GO) was prepared from natural graphite flake via modified Hummer's method [27]. In a typical synthesis, 9 g of graphite flake was added in 20 ml of sulfuric acid (98%), and the mixture was sonicated to create a fine dispersion. Afterwards, this suspension was heated for 4 h at70 °C under magnetic stirring. 20 g of potassium permanganate was appended leisurely to the mixture during the stirring process. The solution was cooled to below 10 °C. Furthermore, the solution was stirred under ice water bath for two hours. This mixture was diluted with distilled water and reacted with10 ml of hydrogen peroxide (20%) and was kept undisturbed for 12 h for residue. The mixture GO solution was rinsed several times with hydrochloric acid and distilled water using a centrifuge.

Synthesis of the $MnFe_2O_4$@ZnO nanoparticles

$MnFe_2O_4$@ZnO nanoparticles were synthesized by facile co-precipitation procedure. Firstly, two transparent solutions were attained when 4.75 g of $Mn(NO_3)_2.4H_2O$ and 5.87 g of $Fe(NO_3)_2 \cdot 9H_2O$ dissolved in 40 ml of distilled water were blended under magnetic stirring for 10 min at ambience temperature. Next, 25% NH_4OH was added dropwise into solution and a dark brown suspension was created. The Mn–Fe precursor was retained under magnetic stirring for 15 min. Moreover, 1 g of $Zn(NO_3)_2.4H_2O$ dissolved in 30 ml of distilled water was blended under magnetic stirring for 10 min. The new blend was stirred for 30 min in the dark at 90 °C for 2 h after the Mn–Fe precursor solution was added to the suspension. In the next stage, the make residue was filtered and washed with ultrapure water for several times and dried at 70 °C overnight. Ultimately, the residue was calcined at 200 °C for 3 h to form $MnFe_2O_4$@ZnO nanoparticles.

Synthesis of the $ZnFe_2O_4$@MnO nanoparticles

$ZnFe_2O_4$@MnO nanoparticles are prepared by a co-precipitation procedure [28]. In this consideration, 3.75 g $Zn(NO_3)_2$ and 4.87 g $Fe(NO_3)_3$ dissolved in 40 ml of distilled water were blended under magnetic stirring for 10 min. Afterwards, 20% NaOH was added dropwise into solution and the pH level was maintained above 10 under stirring for 15 min. Then, a dark brown suspension was made. In addition, 1 g of MnO was calcined at 400 °C for 5 h. Next, the calcined MnO was added to 20% NaOH solution and magnetically stirred for 10 min. Then the Zn–Fe precursor solution was combined to the suspension, the new blend was stirred for 30 min in the dark at 90 °C for 1 h. In the subsequent stage, the created residue was filtered and washed with ultrapure water for some times and dried at 70 °C overnight. Eventually, the residue was calcined at 500 °C for 3 h to form $ZnFe_2O_4$@MnO nanoparticles.

Synthesis of the $ZnFe_2O_4$@MnO/GO and $MnFe_2O_4$@ZnO/GO nanocomposites

The hydrothermal procedure was applied to synthesize the $ZnFe_2O_4$@MnO-graphene oxide and $MnFe_2O_4$@ZnO- graphene oxide nanocomposites [26]. 1000 mg of GO was dispersed in 50 ml of ultrapure water with ultrasonication for 1 h to form a stable GO mixture, and after 200 mg $ZnFe_2O_4$@MnO and $MnFe_2O_4$@ZnO nanocomposites was added and the mixture stirred for30 min at room temperature to prepare a $ZnFe_2O_4$@MnO–GO and $MnFe_2O_4$@ZnO–GO solution. The suspension was transferred to a 100 ml Teflon-lined stainless-steel autoclave and heated to 200 °C for 5 h under autogenous pressure. The reaction suspension was allowed to cool to room temperature and the precipitation was filtered rinsed with ultrapure water and ethanol. Then precipitations were dried in a vacuum oven at 60 °C for 12 h.

Photocatalytic degradation experiments

Photocatalytic activities of graphene oxide/reduced graphene oxide nanocomposites were measured by monitoring the degradation rate of CR solution [25]. For to provide desired visible light, a batch system was applied to carry out the photocatalytic degradation of CR (Fig.1 displays the chemical formula of CR). 0.10 g L^{-1} of graphene oxide/reduced graphene oxide nanocomposites under irradiation of 5 W white LED lamps. The photocatalytic experiments were done at 25 °C with a concentration of 0. 10 g L^{-1} catalysts and 10 mg L^{-1} of CR solution with time intervals of (5–35

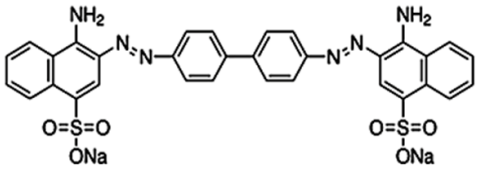

Fig. 1. The chemical formula of CR.

min) at pH= 4. In this experiment, 0.10 g L^{-1} of $ZnFe_2O_4$@MnO, $MnFe_2O_4$@ZnO, $MnFe_2O_4$@ZnO–GO and $ZnFe_2O_4$@MnO-GO nanocomposites was appended to 100 ml of (10 mg L^{-1}) CR solution. Before the photocatalytic action, the mixture was stirred in the dark for 30 min for adsorption–desorption equilibrium between the photocatalyst and dye solution. Eventually, it was irradiated. During irradiation, 5 mL of the mixture was sampled at an interval of 5 min and centrifuged to eliminate the catalyst particles and it was determined by Shimadzu UV-1650PC Model UV-Vis spectrophotometer at λ_{max}= 500 nm. The dye degradation percentage was created from the following equation:

$$R = (C_0 - C) / C_0 \times 100 \quad (1)$$

Where C_0 represents the initial CR concentration (mg/L) and C indicates the CR concentration at a certain reaction time (min). The kinetic studies were done at 25 °C with a concentration range of 0. 10 g L^{-1}, 0.05 g L^{-1} and 0.020 g L^{-1} $MnFe_2O_4$@ZnO–GO and $ZnFe_2O_4$@MZnO-GO nanocomposites and 10 mg L^{-1} of CR solution with times intervals of (5–35 min) at pH= 4.

RESULTS AND DISCUSSION

Structural study

XRD patterns of the samples were determined in ambient air by using a Philips Xpert XRD. Fig. 2 and Fig. 3 illustrate the X-ray diffraction patterns of the as-synthesized $ZnFe_2O_4$@MnO-GO, $ZnFe_2O_4$@MnO-rGO, GO, rGO, pure $ZnFe_2O_4$@MnO, $MnFe_2O_4$@ZnO and $MnFe_2O_4$@ZnO–GO in the 2θ ranges from 5 to 80°. The average crystallite size for $ZnFe_2O_4$@MnO-GO, $ZnFe_2O_4$@MnO-rGO and pure $ZnFe_2O_4$@MnO from the range of 20-40 nm and the average crystallite size for $MnFe_2O_4$@ZnO-GO, $MnFe_2O_4$@ZnO-rGO and pure $MnFe_2O_4$@ZnO from the range of 20-60 nm were calculated by using standard Debye-Scherer equation D= 0.9λ/(βcosθ) [29], where D indicates the diameter of the nanoparticles, λ (Cu Kα) = 1.5406 A° and β represents the full-width at half maximum of the diffraction lines. Fig. 2 demonstrates the X-ray diffraction pattern of the GO, pure $ZnFe_2O_4$@MnO and $ZnFe_2O_4$@MnO-GO, respectively. As shown in Fig. 2a, GO diffraction peaks at the angles of 11.89, 26.61, 44.39 and 77.24° indicated (001), (002), (101) and (110) respectively, which certified the hexagonal phase and were directly accordance with standard (JCPDS No.00-041-1487). The X-ray diffraction pattern of GO shows an intense and sharp peak centred at 11.89° which corresponds to an interplanar distance of 0.82 nm. The increase in interplanar distance of GO is owing to the existence of oxygen functional groups and some other structural flaws. The detectable (002) peak of graphite at 26.61° has an interplanar distance of 0.334 nm. This indicates that graphite is a very oriented carbon material. Also, two other peaks at 44.39° and 77.24° imply the crystalline structure of graphite. The X-ray diffraction pattern of $ZnFe_2O_4$@MnO was shown in Fig. 2b. The peaks centered at the angles of 18.24, 57.42 and 75.50° indicated (111), (511) and (171) respectively, corresponds to $ZnFe_2O_4$@MnO. Based on the results, The peaks centered at the angles of 35.34, 56.79, 62.36 and 73.76° indicated (311), (511), (400) and (533) concurred to the cubic phase of $ZnFe_2O_4$ which were directly indexed to JCPDS No. 98-003-0547. The peaks centered at the angles of 29.96, 33.52, 37.88, 42.19, 57.84, 64.43and 65.38° indicated (023), (113), (006), (220), and (212) agreed to the cubic phase of MnO which were directly indexed to JCPDS No. 01-075-0257. Fig. 2c displays the X-ray diffraction pattern of the $ZnFe_2O_4$@MnO-GO. The peaks centered at the angles of 26.45, 29.87 and 43.41° corresponded to GO, $ZnFe_2O_4$@MnO-GO and $ZnFe_2O_4$@MnO, respectively. On the other, during the hydrothermal reaction, crystal growth of $ZnFe_2O_4$@MnO between the interplay of GO damaged the regular layer stacking, making to the exfoliation of GO and the disappearance of the (001) diffraction peak [25]. Fig. 3 demonstrates the X-ray diffraction pattern of the GO, pure $MnFe_2O_4$@ZnO and $MnFe_2O_4$@ZnO-GO, respectively. As shown in Fig. 3a, GO diffraction

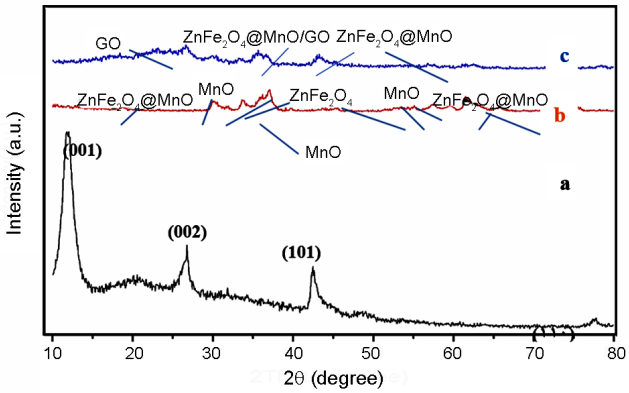

Fig. 2. XRD patterns for (a) GO (b) $ZnFe_2O_4$@MnO and (c) $ZnFe_2O_4$@MnO/GO.

peaks were observed at 11.89, 26.61, 44.39and 77.24° which corresponds to the (001), (002), (101) and (110) respectively. These diffraction peaks confirmed the hexagonal phase and were directly accordance with standard (JCPDS No.00-041-1487). The X-ray diffraction pattern of GO displays a sharp peak centred at 10.89° which corresponds to an interplanar distance of 0.82 nm. An increased interlayer distance between consecutive carbon basal planes is ascribed to the intercalation of oxygen functional groups and water molecules into carbon layer structure. The detectable peak of graphite at 26.61°, corresponding to the highly organized layer structure with an interlayer distance of 0.34 nm along the (002) orientation. Also, two other peaks at 44.39° and 77.24° confirm the crystalline structure of graphite. The X-ray diffraction pattern of $MnFe_2O_4$@ZnO was shown in Fig. 3b. The peaks centered at the angles of 35. 39, 42.93 and 62.30° indicated (113), (004) and (022) respectively, which corresponded to $MnFe_2O_4$@ZnO. Based on the results, The

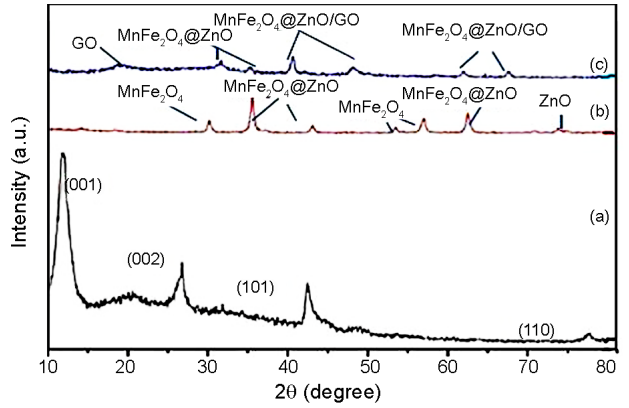

Fig. 3. XRD patterns for (a) GO, (b) $MnFe_2O_4$@ZnO and (c) $MnFe_2O_4$@ZnO/GO.

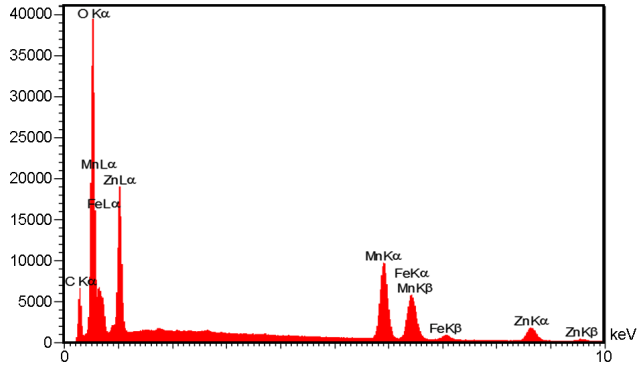

Fig. 4. EDAX analyses of $ZnFe_2O_4$@MnO-GO nanocomposite.

peaks centered at the angles of 18.23, 29.99, 35.33, 53.26, 56.77, 70.71 and 74.73° indicated (111), (022), (113), (224), (115), (026) and (226) agreed to the cubic phase of $MnFe_2O_4$ which were directly indexed to JCPDS No. 98-006-2998. The peaks centered at the angles of 36.94, 42.92, 62.31, 74.70 and 78.64° indicated (111), (002), (022), (113) and (222) agreed to the cubic phase of ZnO which were directly indicated to JCPDS No. 98-011-6320. Fig. 3c explains the X-ray diffraction pattern of the $MnFe_2O_4$@ZnO-GO. The peaks centered at the angles of 35.45, 53.38, 56.83, 62.46 and 73.90° corresponded to $MnFe_2O_4$@ZnO-GO and also, these diffraction peaks centered at the angles of 30.13° and 43.02° corresponded to $MnFe_2O_4$@ZnO and one diffraction peak was showed at 13.59° which corresponds to graphene oxide. On the other, During the hydrothermal process in reaction, crystal growth of $MnFe_2O_4$@ZnO between the interplay of graphene oxide nanosheet mortified the regular layer stacking, which is leading to the exfoliation of GO and the disappearance of the (001) diffraction peak [26].

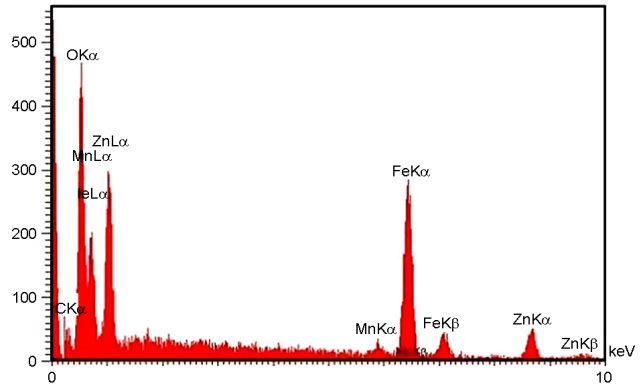

Fig. 5. EDAX analyses of $MnFe_2O_4$@ZnO-GO nanocomposite.

Table 1. EDX quantification elements of $ZnFe_2O_4$@MnO-GO nanocomposite.

Element	C	O	Mn	Fe	Zn	Total
W%	12.54	33.94	25.60	13.28	14.65	100.00
Atom%	25.50	51.83	11.39	5.81	5.47	100.00

Table 2. EDX quantification elements of $MnFe_2O_4$@ZnO-GO nanocomposite

Element	C	O	Mn	Fe	Zn	Total
W%	8.84	33.88	1.32	39.39	16.58	100.00
Atom%	19.18	55.20	0.63	18.38	6.61	100.00

As illustrated in Fig. 4 and Fig. 5, the EDAX data for the nanocatalyst $ZnFe_2O_4$@MnO-GO and $MnFe_2O_4$@ZnO-GO could confirm the presence of C, Zn, Fe, Mn and O elements in synthesized photocatalysts, respectively. The amounts of elements are reported for the nanocatalyst $ZnFe_2O_4$@MnO-GO and $MnFe_2O_4$@ZnO-GO in Tables 1 and 2, respectively. Further, 6b and 7b display the agglomerated spherical shape of $ZnFe_2O_4$@MnO and $MnFe_2O_4$@ZnO-GO nanoparticles with an average particle size of < 100 nm. Furthermore, it can be shown that the spherical shape of $ZnFe_2O_4$@MnO nanoparticles was unequally decorated on the surface of the GO sheet with an average particle size of < 100 nm in Fig. 6c, d. Fig. 7a reveals the formation of a multi-layered of GO nanosheet, Furthermore, It can be shown that the spherical shape of $MnFe_2O_4$@ZnO nanoparticles was unequally decorated on the surface of the GO sheet with an average particle size of < 100 nm in Fig. 7c, d. TEM images of the $ZnFe_2O_4$@MnO-GO nanocomposites are shown in Figs 7. It can be clearly shown that the microstructure of $ZnFe_2O_4$@MnO-GO samples display the agglomerated spherical $ZnFe_2O_4$@MnO nanoparticles, which are randomly dispersed over the surface of GO nanosheets as shown in Fig. 7. And so, the dark gray nanoparticles ($ZnFe_2O_4$) were dispersed on the surface of light gray nanoparticles (MnO) as shown in Figs 7. Furthermore, the microstructure of $MnFe_2O_4$@ZnO-GO was examined by using TEM analysis in Figs 9. It can be clearly shown that the microstructure of $MnFe_2O_4$@ZnO-GO nanocomposites display the agglomerated spherical $MnFe_2O_4$@ZnO nanoparticles,

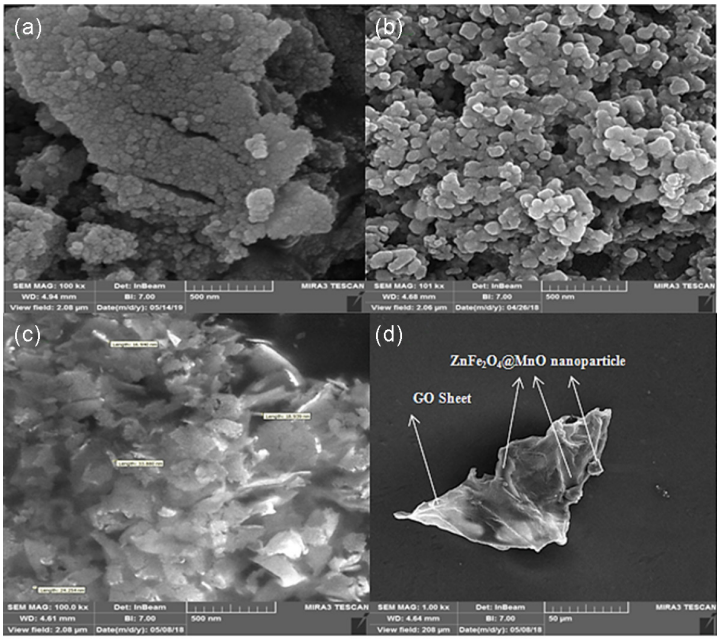

Fig. 6. (a) FESEM image of GO sheets, (b) $ZnFe_2O_4$@MnO nanoparticles, (c) and (d) $ZnFe_2O_4$@MnO-GO nanocomposites.

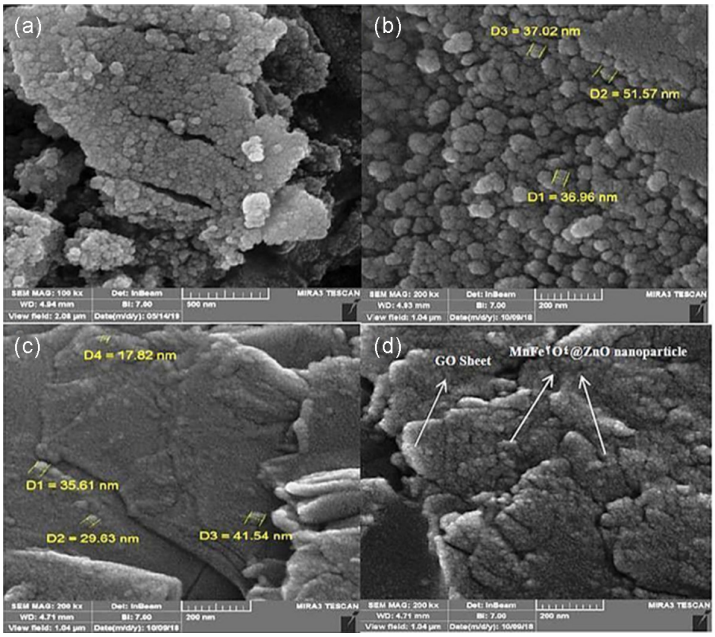

Fig. 7. a FESEM image of GO sheets, b $MnFe_2O_4$@ZnO nanoparticles, c, d $MnFe_2O_4$@ZnO-GO nanocomposites.

which are randomly dispersed over the surface of GO nanosheets as shown in Fig. 9. In addition, the dark gray nanoparticles ($MnFe_2O_4$) were dispersed on the surface of light gray nanoparticles (ZnO) as shown in Figs 7 and 8 [26].

Porosity and Surface Chemistry of $ZnFe_2O_4$@MnO-GO and $MnFe_2O_4$@ZnO -GO

The nitrogen adsorption–desorption isotherms were performed in order to carry out an analysis relevant to the porosity properties of $ZnFe_2O_4$@MnO-GO and $MnFe_2O_4$@ZnO-GO, and the further interpretation was performed by using Brunauer–Emmett–Teller (BET) method. Total pore volume, average pore diameters and surface area of synthesized samples, for evaluation of porosity and surface chemistry are listed in Table 3. Figs 10 and 11 display the N_2 adsorption isotherm and pore size distribution curve of synthesized $ZnFe_2O_4$@MnO-GO and $MnFe_2O_4$@ZnO -GO nanocomposites. The isotherms show the features of type IV isotherms according to IUPAC classification, indicating the presence of mesopores structures in the samples. The specific surface area of $ZnFe_2O_4$@MnO-GO and $MnFe_2O_4$@ZnO-GO nanocomposites are 26.77 m^2/g and 26.34 m^2/g with an average pore size diameter of 18.03 nm and 9.18 nm, respectively, which significantly determines the mesoporous nature. While the surface area of $ZnFe_2O_4$@MnO nanoparticles, GO and $MnFe_2O_4$@ZnO nanoparticles are found to be

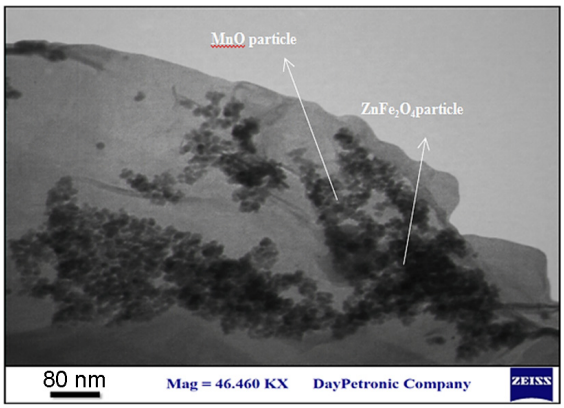

Fig. 8. TEM images of the $ZnFe_2O_4$@MnO-GO nanocomposites.

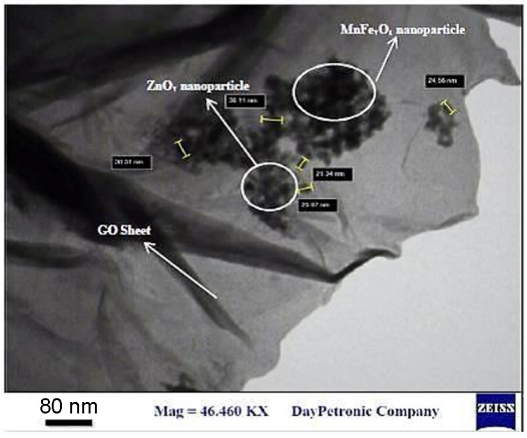

Fig. 9. TEM images of the $MnFe_2O_4$@ZnO-GO nanocomposites.

Table 3. BET analysis of GO, $ZnFe_2O_4$@MnO, $ZnFe_2O_4$@MnO-GO, $MnFe_2O_4$@ZnO and$MnFe_2O_4$@ZnO-GO nanocomposites.

Samples	Surface Area (m^2/g)	Total Pore Volume (cm^3/g)	Average Pore Diameter (nm)
GO	5.86	0.03722	25.37
$ZnFe_2O_4$@MnO	75.54	0.203	10.74
$ZnFe_2O_4$@MnO-GO	26.77	0.1207	18.03
$MnFe_2O_4$@ZnO	125.77	0.2218	7.05
$MnFe_2O_4$@ZnO-GO	26.34	0.06631	9.18

75.54 m^2/g, 5.86 m^2/g and 125.77 m^2/g with an average pore size of 10.74 nm, 25.37 nm and 7.05 nm, respectively, as given in Table 3 [25, 26]. The lower surface area of Zn@MnO-GO and $MnFe_2O_4$@ZnO-GO nanocomposites compared to the $ZnFe_2O_4$@MnO and $MnFe_2O_4$@ZnO may be owing to blocking of a few sites by GO in the $ZnFe_2O_4$@MnO and $MnFe_2O_4$@ZnO structure [26]. On the other hand, the surface area of the catalyst is one of the most important factors in photodegradation processes, higher surface area of the catalyst, causes the generation of more active species and improvement of the photocatalytic performance [30]. The higher the surface area of synthesized $ZnFe_2O_4$@MnO-GO and $MnFe_2O_4$@ZnO-GO compared to the $ZnFe_2O_4$@MnO and $MnFe_2O_4$@ZnO, causes the generation improvement of the photocatalytic activity of the synthesized $ZnFe_2O_4$@MnO-GO and $MnFe_2O_4$@ZnO-GO nanocomposite compared to $ZnFe_2O_4$@MnO and $MnFe_2O_4$@ZnO nanocomposites under the visible light.

Photocatalytic performance of $MnFe_2O_4$@ZnO-GO and $ZnFe_2O_4$@MnO-GO

The photocatalytic efficiency of synthesized $MnFe_2O_4$@ZnO, $MnFe_2O_4$@ZnO-GO, $ZnFe_2O_4$@MnO and $ZnFe_2O_4$@MnO-GO nanocomposites was evaluated by using CR dye solutions as a model pollutant under natural sunlight irradiation for time intervals

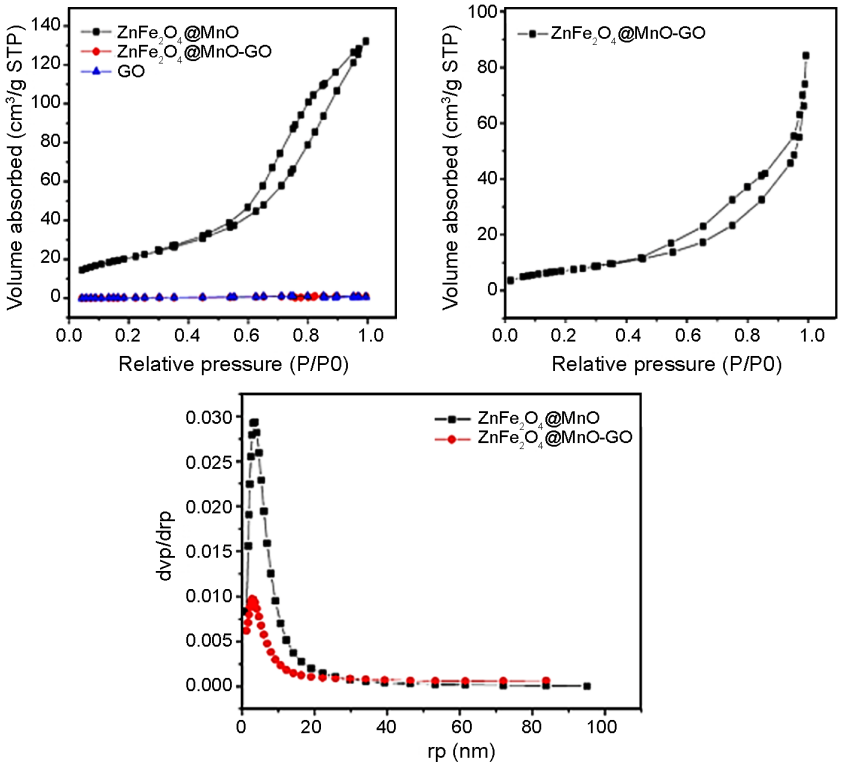

Fig. 10. N_2 adsorption isotherms of GO, $ZnFe_2O_4$@MnO and $ZnFe_2O_4$@MnO-GO nanocomposites along with pore size distribution curve.

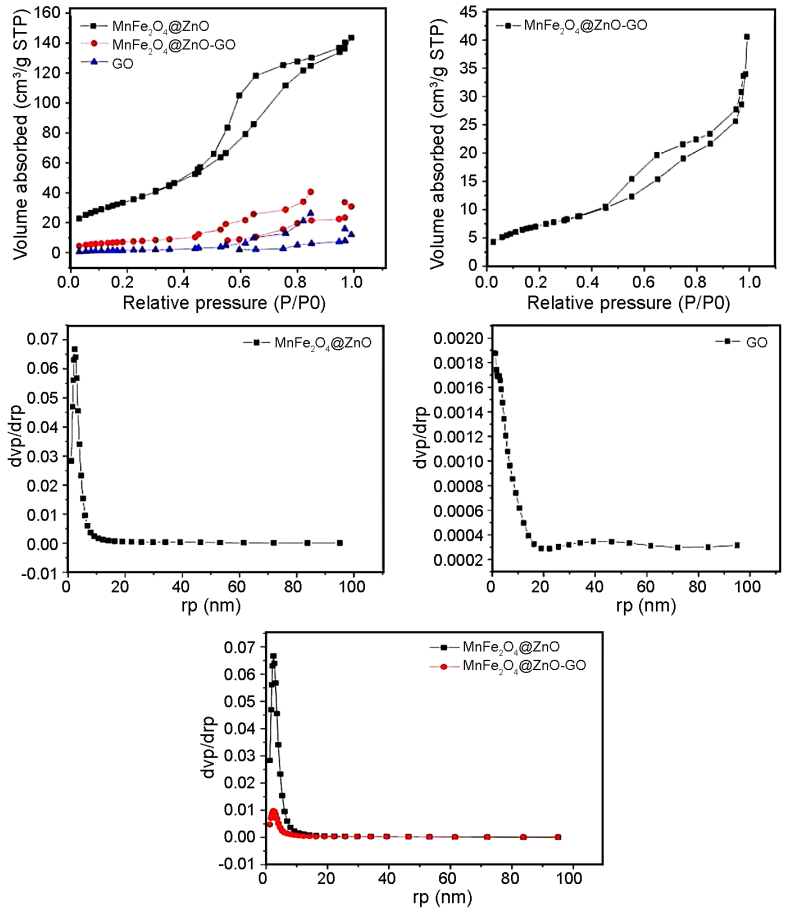

Fig. 11. N_2 adsorption isotherms of GO, $MnFe_2O_4$@ZnO and $MnFe_2O_4$@ZnO-GO nanocomposites along with pore size distribution curve.

of (5–35 min) at pH= 3 for $MnFe_2O_4$@ZnO and $MnFe_2O_4$@ZnO-GO nanocomposites and pH=4 for $ZnFe_2O_4$@MnO and $ZnFe_2O_4$@MnO-GO nanocomposites, as shown in Figs 12, 13, 14 and 15. In this regard, 100 ml of 10 mg/l CR solution in the presence of 0.10 g $MnFe_2O_4$@ZnO, $MnFe_2O_4$@ZnO-GO, $ZnFe_2O_4$@MnO and $ZnFe_2O_4$@MnO-GO nanocomposites were exhibited to the sunlight irradiation. The degradation rate was carried out by decreasing in peak intensity at

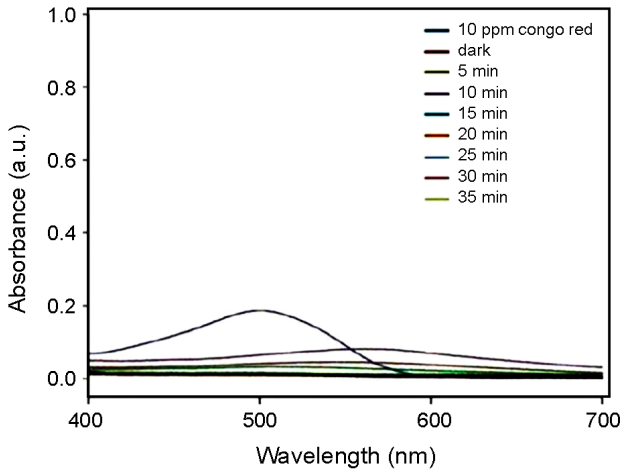

Fig. 12. Photocatalytic degradation of Congo red under visible light in presence of $MnFe_2O_4$@ZnO.

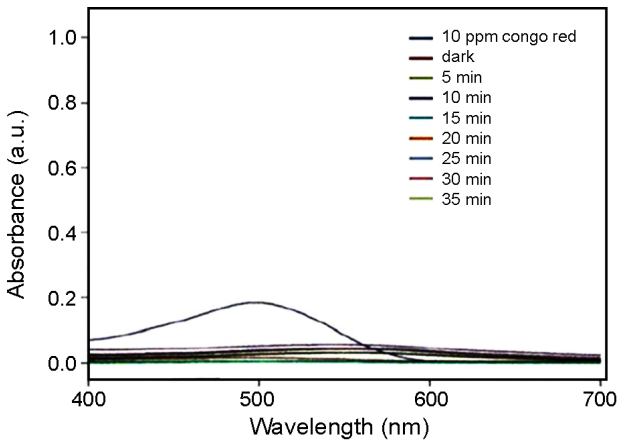

Fig. 13. Photocatalytic degradation of Congo red under visible light in presence of MnFe2O4@ZnO-GO.

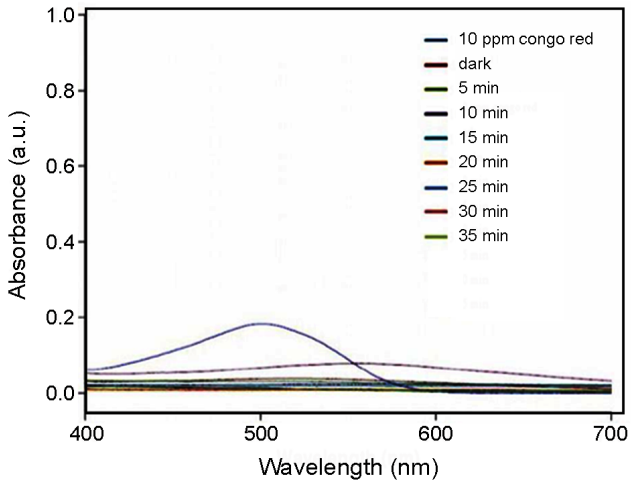

Fig. 14. Photocatalytic degradation of Congo red under visible light in presence of $ZnFe_2O_4$@MnO.

498 nm in Figs 12, 13 14 and 15. When $MnFe_2O_4$@ZnO, $MnFe_2O_4$@ZnO-GO, $ZnFe_2O_4$@MnO and $ZnFe_2O_4$@MnO-GO nanocomposites are added into solution and exposed to sunlight for 35 minutes, peak intensity regularly decreases. The results indicated that the percentage of maximum dye degradation in the presence of 0.10 g $MnFe_2O_4$@ZnO, $MnFe_2O_4$@ZnO-GO, $ZnFe_2O_4$@MnO and $ZnFe_2O_4$@MnO-GO nanocomposites were 92.32%, 99.54%, 96.21% and 98.73% respectively [25, 26]. It is clearly observed, that the intensity of absorption peaks decreased for $MnFe_2O_4$@ZnO-GO and $ZnFe_2O_4$@MnO-GO much more than that of $MnFe_2O_4$@ZnO and $ZnFe_2O_4$@MnO at 498nm (i.e. wave length of CR absorption) along with the increase in the irradiation time. Degradation efficiency of CR dye by $MnFe_2O_4$@ZnO-GO (99.54% in 35 min) and $ZnFe_2O_4$@MnO-GO (98.73% in 35 min) were greater than that of $MnFe_2O_4$@ZnO

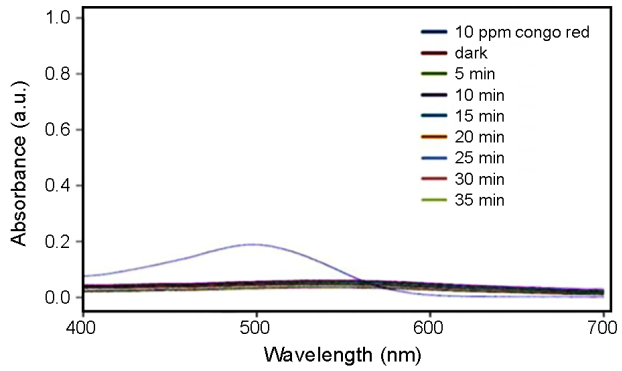

Fig. 15. Photocatalytic degradation of Congo red under visible light in presence of $ZnFe_2O_4$@MnO-GO.

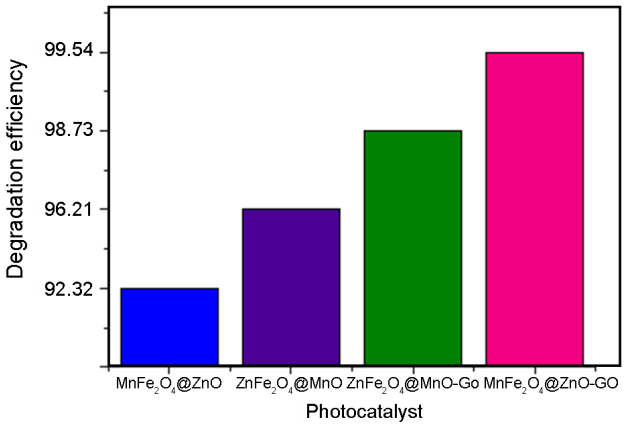

Fig. 16. Comparison of the photodegradation efficiencies of Congo red for $ZnFe_2O_4$@MnO, $ZnFe_2O_4$@MnO-GO, $MnFe_2O_4$@ZnO and $MnFe_2O_4$@ZnO-GO nanocomposites under visible light irradiation for 35 min.

(92.32% in 35 min) and $ZnFe_2O_4$@MnO samples (96.21% in 35 min). It could be due to the narrower band gap in presence of incorporated GO in the structure of $MnFe_2O_4$@ZnO and $ZnFe_2O_4$@MnO nanocomposites. This phenomenon can be explained that GO acts as a photosensitizer for $MnFe_2O_4$@ZnO and $ZnFe_2O_4$@MnO instead of an electron reservoir in the photocatalytic mechanism in the structure of $MnFe_2O_4$@ZnO-GO and $ZnFe_2O_4$@MnO-GO nanomaterials. The photocatalytic degradation of Congo red as a function of time by employing the synthesized $ZnFe_2O_4$@MnO, $ZnFe_2O_4$@MnO-GO, $MnFe_2O_4$@ZnO and $MnFe_2O_4$@ZnO-GO nanocomposites was studied under visible light irradiation, as shown in Figs 26. It can be demonstrated that the $ZnFe_2O_4$@MnO-GO nanocomposites compared to $ZnFe_2O_4$@MnO nanocomposites gave the best efficiency in the photocatalytic degradation of Congo red. Also, it can be indicated that the $MnFe_2O_4$@ZnO-GO nanocomposites compared to $MnFe_2O_4$@ZnO nanocomposites gave the best efficiency in the photocatalytic degradation of Congo red. The $MnFe_2O_4$@ZnO-GO and $ZnFe_2O_4$@MnO-GO nanocomposites gave the highest photocatalytic efficiency due to the well optical absorptions in the UV-Vis region with lower band gap energy and a larger surface area giving a rise to a higher photocatalytic activity. Additionally, the graphene oxide in the nanocomposite can act as an electron transfer channel to reduce the recombination of the photo-generated electron holes, leading to improved performance pho-

to-conversion efficiency [31, 32]. In addition, it can be indicated that the $MnFe_2O_4$@ZnO-GO nanocomposites compared to $ZnFe_2O_4$@MnO-GO nanocomposites gave the best efficiency in the photocatalytic degradation of Congo red. In relevance to structure photoactivity of $MnFe_2O_4$@ZnO-GO nanocomposite, we propose a photocatalytic mechanism where the role of GO in the $MnFe_2O_4$@ZnO-GO nanocomposites acts as an "electron transport channel" for $MnFe_2O_4$@ZnO instead of an electron reservoir, therefore creating they reveal visible light photoactivity.

CONCLUSIONS

In the present study, hydrothermal method was used as a simple and straightforward synthesis method to successfully synthesize $MnFe_2O_4$@ZnO-GO and $ZnFe_2O_4$@MnO-GO metal oxide-organic framework nanocomposites with various GO contents. And also, a facile co-precipitation approach was used for synthesizing $MnFe_2O_4$@ZnO and $ZnFe_2O_4$@MnO nanocomposites with the larger surface area, unique morphology. The photocatalytic performance results indicated that $MnFe_2O_4$@ZnO, $MnFe_2O_4$@ZnO-GO, $ZnFe_2O_4$@MnO and $ZnFe_2O_4$@MnO-GO degrade Congo red dye in the same reaction condition by 92.32 %, 99.54 %, 96.21% and 98.73% respectively. Our proposed $MnFe_2O_4$@ZnO-GO and $ZnFe_2O_4$@MnO-GO photocatalyst displayed a relatively considerable photocatalytic capability compared to that of pure $MnFe_2O_4$@ZnO and $ZnFe_2O_4$@MnO catalysts to degrade CR as a hazardous pollutant under natural sunlight in 35 minutes. It has been indicated that the visible-light-driven photocatalytic oxidation process for $MnFe_2O_4$@ZnO-GO and $ZnFe_2O_4$@MnO-GO results from a GO photosensitization of $MnFe_2O_4$@ZnO and $ZnFe_2O_4$@MnO, for which upon visible light irradiation no holes are produced due to the wide band gap of $MnFe_2O_4$@ZnO and $ZnFe_2O_4$@MnO not able to be photoexcited by visible light irradiation. The photocatalytic behavior was improved, since the photo-induced pairs of electron and hole had a low rate of recombination. The combination of the adsorption property of the graphene oxide nanosheet, the magnetic property and GO electron transport property in the $MnFe_2O_4$@ZnO-GO and $ZnFe_2O_4$@MnO-GO nanocomposites compared to $MnFe_2O_4$@ZnO and $ZnFe_2O_4$@MnO nanocomposites makes the photocatalyst promising candidates for the solution of a variety of environmental problems. Moreover, it can be demonstrated that the $MnFe_2O_4$@ZnO-GO nanocomposites compared to $ZnFe_2O_4$@MnO-GO nanocomposites gave the best performance in the photocatalytic degradation of Congo red owing to structure photoactivity of $MnFe_2O_4$@ZnO-GO nanocomposite because of the role of GO in the $MnFe_2O_4$@ZnO-GO nanocomposites performs as an "electron transport channel" for $MnFe_2O_4$@ZnO instead of an electron reservoir, therefore creating they show visible light photoactivity. We also hope that our work be used for other metal oxide combined with GO, and the role of frameworks with different morphologies be considered for controlling other pollutants.

ACKNOWLEDGEMENT

We thank science and research Branch, Islamic Azad University Tehran for supporting this study and Iran Nanotechnology Initiative.

REFERENCES

[1] Mohamed, M. M., Osman, G., & Khairou, K. S. (2015). Fabrication of Ag nanoparticles modified TiO_2–CNT heterostructures for enhanced visible light photocatalytic degradation of organic pollutants and bacteria. Journal of Environmental Chemical Engineering, 3(3), 1847-1859.

[2] Atar, N., Olgun, A., Wang, S., & Liu, S. (2011). Adsorption of anionic dyes on boron industry waste in single and binary solutions using batch and fixed-bed systems. Journal of Chemical & Engineering Data, 56(3), 508-516.

[3] Gupta, V. K., Yola, M. L., & Atar, N. (2014). A novel molecular imprinted nanosensor based quartz crystal microbalance for determination of kaempferol. Sensors and Actuators B: Chemical, 194, 79-85.

[4] Alinsafi, A., Evenou, F., Abdulkarim, E. M., Pons,

M. N., Zahraa, O., Benhammou, A., & Nejmeddine, A. (2007). Treatment of textile industry wastewater by supported photocatalysis. Dyes and Pigments, 74(2), 439-445.

[5] Xu, Y., Xu, H., Li, H., Xia, J., Liu, C., & Liu, L. (2011). Enhanced photocatalytic activity of new photocatalyst Ag/AgCl/ZnO. Journal of Alloys and Compounds, 509(7), 3286-3292.

[6] Firooz, A. A., Mahjoub, A. R., Khodadadi, A. A., & Movahedi, M. (2010). High photocatalytic activity of Zn2SnO4 among various nanostructures of Zn2xSn1−xO2 prepared by a hydrothermal method. Chemical Engineering Journal, 165(2), 735-739.

[7] Yassıtepe, E., Yatmaz, H. C., Öztürk, C., Öztürk, K., & Duran, C. (2008). Photocatalytic efficiency of ZnO plates in degradation of azo dye solutions. Journal of Photochemistry and Photobiology A: Chemistry, 198(1), 1-6.

[8] Walker, G. M., & Weatherley, L. R. (1997). Adsorption of acid dyes on to granular activated carbon in fixed beds. Water Research, 31(8), 2093-2101.

[9] Acemioğlu, B. (2004). Adsorption of Congo red from aqueous solution onto calcium-rich fly ash. Journal of Colloid and Interface Science, 274(2), 371-379.

[10] Sinthiya, M. M. A., Ramamurthi, K., Mathuri, S., Manimozhi, T., Kumaresan, N., Margoni, M. M., & Karthika, P. C. (2015). Synthesis of zinc ferrite ($ZnFe_2O_4$) nanoparticles with different capping agents. Int. J. Chem. Tech. Res, 7, 2144-2149.

[11] Gurumoorthy, M., Parasuraman, K., Anbarasu, M., & Balamurugan, K. (2015). FT-IR. XRD and SEM study of $MnFe_2O_4$ nanoparticles by chemical co-precipitation method, Nano Vision, 5, 63-68.

[12] Cui, L., Guo, P., Zhang, G., Li, Q., Wang, R., Zhou, M., & Zhao, X. S. (2013). Facile synthesis of cobalt ferrite submicrospheres with tunable magnetic and electrocatalytic properties. Colloids and Surfaces A: Physicochemical and Engineering Aspects, 423, 170-177.

[13] Goodarz Naseri, M., Saion, E. B., Abbastabar Ahangar, H., Shaari, A. H., & Hashim, M. (2010). Simple synthesis and characterization of cobalt ferrite nanoparticles by a thermal treatment method. Journal of Nanomaterials, 2010.

[14] Choi, K., Kang, T., & Oh, S. G. (2012). Preparation of disk shaped ZnO particles using surfactant and their PL properties. Materials Letters, 75, 240-243.

[15] Zhang, H., Lv, X., Li, Y., Wang, Y., & Li, J. (2010). P25-graphene composite as a high performance photocatalyst. ACS Nano 4: 380–386.

[16] Sun, L., Li, J., Wang, C., Li, S., Lai, Y., Chen, H., & Lin, C. (2009). Ultrasound aided photochemical synthesis of Ag loaded TiO_2 nanotube arrays to enhance photocatalytic activity. Journal of Hazardous Materials, 171(1-3), 1045-1050.

[17] Ai, Z., Ho, W., Lee, S., & Zhang, L. (2009). Efficient photocatalytic removal of NO in indoor air with hierarchical bismuth oxybromide nanoplate microspheres under visible light. Environmental Science & Technology, 43(11), 4143-4150.

[18] Huang, L., Peng, F., Wang, H., Yu, H., & Li, Z. (2009). Preparation and characterization of Cu2O/TiO_2 nano–nano heterostructure photocatalysts. Catalysis Communications, 10(14), 1839-1843.

[19] Mzoughi, M., Anku, W., OB Oppong, S., K Shukla, S., S Agorku, E., & P Govender, P. (2016). Neodymium doped ZrO_2-graphene oxide nanocomposites: a promising photocatalyst for photodegradation of Eosin Y dye. Advanced Materials Letters, 7(12), 946-950.

[20] Kooshki, H., Sobhani-Nasab, A., Eghbali-Arani, M., Ahmadi, F., Ameri, V., & Rahimi-Nasrabadi, M. (2019). Eco-friendly synthesis of PbTiO3 nanoparticles and PbTiO3/carbon quantum dots binary nano-hybrids for enhanced photocatalytic performance under visible light. Separation and Purification Technology, 211, 873-881.

[21] Sobhani-Nasab, A., Behpour, M., Rahimi-Nasrabadi, M., Ahmadi, F., Pourmasoud, S., & Sedighi, F. (2019). Preparation, characterization and investigation of sonophotocatalytic activity of thulium titanate/polyaniline nanocomposites in degradation of dyes. Ultrasonic Sonochemistry, 50, 46-58.

[22] Sedighi, F., Esmaeili-Zare, M., Sobhani-Nasab, A., & Behpour, M. (2018). Synthesis and characterization of $CuWO_4$ nanoparticle and $CuWO_4$/

NiO nanocomposite using co-precipitation method; application in photodegradation of organic dye in water. Journal of Materials Science: Materials in Electronics, 29(16), 13737-13745.

[23] Eghbali-Arani, M., Sobhani-Nasab, A., Rahimi-Nasrabadi, M., Ahmadi, F., & Pourmasoud, S. (2018). Ultrasound-assisted synthesis of $YbVO_4$ nanostructure and $YbVO_4$/$CuWO_4$ nanocomposites for enhanced photocatalytic degradation of organic dyes under visible light. Ultrasonics Sonochemistry, 43, 120-135.

[24] Das, R. S., Warkhade, S. K., Kumar, A., & Wankhade, A. V. (2019). Graphene oxide-based zirconium oxide nanocomposite for enhanced visible light-driven photocatalytic activity. Research on Chemical Intermediates, 45(4), 1689-1705.

[25] Zamani, A., Sadjadi, M. S., Mahjoub, A., Yousefi, M., & Farhadyar, N. (2020). Synthesis, characterization and investigation of photocatalytic activity of $ZnFe_2O_4$@ MnO–GO and $ZnFe_2O_4$@ MnO–rGO nanocomposites for degradation of dye Congo red from wastewater under visible light irradiation. Research on Chemical Intermediates, 46(1), 33-61.

[26] Thakur, A., Kumar, S., & Rangra, V. S. (2015). Synthesis of reduced graphene oxide (rGO) via chemical reduction. In AIP Conference Proceedings, 1661(1), 080032. AIP Publishing LLC.

[27] Suwanchawalit, C., & Somjit, V. (2015). Hydrothermal synthesis of magnetic $CoFe_2O_4$-graphene nanocomposite with enhanced photocatalytic performance. Digest. J. Nanomater. Biostruc, 10, 769-777.

[28] Gupta, V. K., Eren, T., Atar, N., Yola, M. L., Parlak, C., & Karimi-Maleh, H. (2015). $CoFe_2O_4$@ TiO_2 decorated reduced graphene oxide nanocomposite for photocatalytic degradation of chlorpyrifos. Journal of Molecular Liquids, 208, 122-129.

[29] Azam, Z., Sadjadi, M. S., Alireza, M., Mohammad, Y., & Nazanin, F. (2020). Synthesis, characterization and investigation of photocatalytic activity of ZnMnO3/Fe3O4 nanocomposite for degradation of dye Congo red under visible light irradiation. International Journal of Industrial Chemistry, 11(4), 205-216.

[30] Karthik, R., Kumar, J. V., Chen, S. M., Kumar, P. S., Selvam, V., & Muthuraj, V. (2017). A selective electrochemical sensor for caffeic acid and photocatalyst for metronidazole drug pollutant-A dual role by rod-like SrV2O6. Scientific Reports, 7(1), 1-12.

[31] Wang, D., Li, X., Chen, J., & Tao, X. (2012). Enhanced photoelectrocatalytic activity of reduced graphene oxide/TiO_2 composite films for dye degradation. Chemical Engineering Journal, 198, 547-554.

[32] Ullah, K., Zhu, L., Meng, Z. D., Ye, S., Sun, Q., & Oh, W. C. (2013). A facile and fast synthesis of novel composite Pt–graphene/TiO_2 with enhanced photocatalytic activity under UV/Visible light. Chemical Engineering Journal, 231, 76-83.

AUTHOR (S) BIOSKETCHES

Azam Zamani, PhD., Department of Chemistry, Science and Research Branch, Islamic Azad University, Tehran, Iran, *Email: Azamani646@gmail.com*

Mirabdullah Seyed Sadjadi, Professor, Department of Chemistry, Science and Research Branch, Islamic Azad University, Tehran, Iran, *Email: m.s.sadjad@gmail.com*

Alireza Mahjoub, Professor, Department of Chemistry, Tarbiat Modares University, Tehran, Iran, *Email: mahjouba@modares.ac.ir*

Moha-mmad Yousefi, Professor, Department of Chemistry, Science and Research Branch, Islamic Azad University, Tehran, Iran, *Email: myousefi50@hotmail.com*

Nazanin Farhadyar, Associate Professor, Department of Chemistry, Varamin Pishva Branch, Islamic Azad University, Varamin, Iran, *Email:quantomlife@gmail.com*